Electronic Supplementary Material (ESI) for Physical Chemistry Chemical Physics.

Exploring doping or vacancy-modified graphene-based electrodes for applications in asymmetric supercapacitors

Débora A. C. da Silva[1] Antenor J. Paulista Neto,[2] Aline M. Pascon,[1]Eudes E. Fileti[2,]
Leonardo R. C. Fonseca[3] e Hudson G. Zanin[1]

(1) Center for Innovation on New Energies, Advanced Energy Storage Division, Carbon Sci-Tech Labs, University of Campinas, School of Electrical and Computer Engineering, Av. Albert Einstein 400, Campinas - SP, 13083-852, Brazil.
(2) Institute of Science and Technology of the Federal University of São Paulo, 12247-014, São José dos Campos, SP, Brazil.
(3) Department of Physics, Federal University of Minas Gerais, Av. Pres. Antônio Carlos, 6627, Belo Horizonte, MG, 31270-901 Brazil.

SUPPORTING MATERIAL

Due to its peculiar electron density at the Fermi level, defect-free graphene presents quantum capacitance, which arises due to the occupation of higher energy states as the supercapacitor is charged.[1] Unlike metals, which have extremely high quantum capacitance, graphene quantum capacitance is only of the same order as the double-layer capacitance.[1] Assuming that the total capacitance of a graphene supercapacitor is a series connection of double-layer capacitance (C_{EDL}) and quantum capacitance (C_Q) then the total capacitance is: $C_T = \frac{C_{EDL} \times C_Q}{C_{EDL} + C_Q}$. Thus, for the total capacitance to be of high value; it is needed that both contributions must be at the same time comparable and high. According to the Figure S1, these two characteristics must be achieved simultaneously, because if only one value is high, its contribution to total capacitance tends to be negligible, while if both are low, the total capacitance also tends to be low. Some aspects related to this problem have already been investigated in the literature.[2-5]

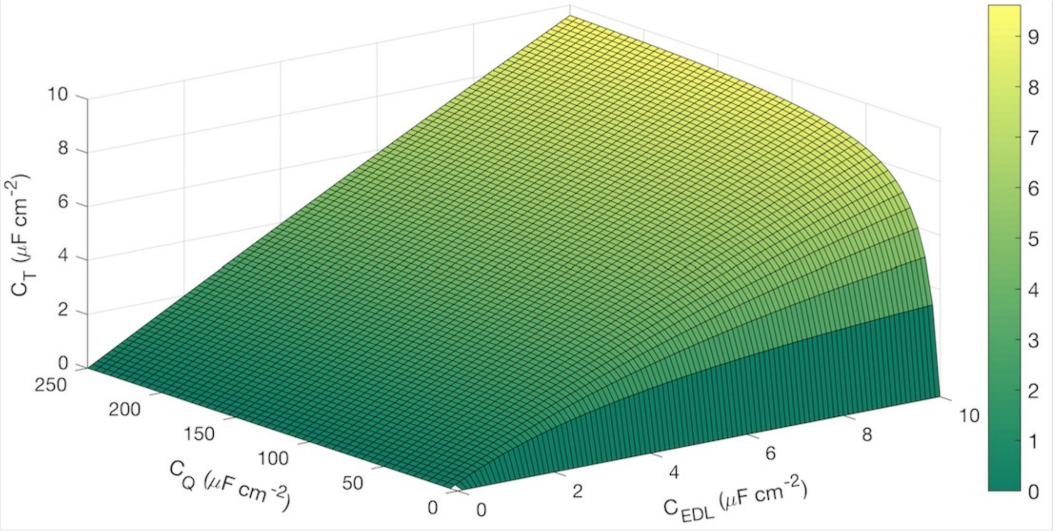

Figure S1: Total capacitance plot as a function of quantum and electric double-layer capacitances.

Further details on the DFTcalculations

The quantum capacitance (C_Q) of graphene was obtained from density of states (DOS), $D(E)$, assuming the fixed band approximation, i.e., the DOS profile is assumed to be not affected by charging/discharging. From $D(E)$ near the Fermi level, we can calculate the quantum capacitance:

$$C_Q = \frac{\partial Q}{\partial \varphi} e^2 \int_{-\infty}^{+\infty} D(E)\left[F_T(E-\varphi)\right] dE \qquad \text{(eq. S1)}$$

where F_T is Fermi-Dirac distribution function, E refers to energy with respect to Fermi level, and e is elementary charge (1.6x10^{-19} C).Here, F_T is given by:

$$F_T(E) = \frac{1}{4K_BT} sech^2\left(\frac{E}{2K_BT}\right) \qquad \text{(eq. S2)}$$

where K_B= 1.38x10^{-23} m^2 kg s^{-2} K^{-1} is Boltzmann´s constant and T is temperature parameter applied (300 K).SoC_Q can be given by:

$$C_Q = \frac{e^2}{4K_BT}\int_{-\infty}^{+\infty} D(E)sech^2\left(\frac{E+\varphi}{2K_BT}\right)dE \quad \text{(eq. S3)}$$

The calculation of C_Q for all graphene configurations is over a potential range -0.6 to 0.6 V, which is the electrochemical window of aqueous electrolytes of a supercapacitor.

The energy stability of graphene was investigated by calculating form energies per unit length of the sheet (E_{FOR}), using an expression below:

$$E_{FOR} = \frac{\left[E_D - xE_C - y\frac{E_{GAS}}{2}\right]}{L}$$

here, E_D, E_C and E_{GAS} refer to the energies of defect sheet, carbon atom of pristine graphene, and doping gas, respectively, x and y indicate the number of carbon and doping atom present in the configuration. L is length of sheet considered (9.9 Å).

Further details on the MD simulations

The systems consisted of two rigid electrodes separated by a distance of ~12nm with a sectional area of 3.4 x 3.4 nm^2. In this slab geometry, the z-axis is defined as the direction normal to the electrodes. The electrolyte composed of 180 Li$^+$, 90 SO_4^{2-} and 5000 water molecules reached the density of the bulk at the center of the supercapacitor. A vacuum slice of 8 nm was inserted between the electrodes in order to minimize their interaction and periodic boundary conditions are applied only in the xy-plane (parallel to the electrodes). All trajectories were produced at NVT ensemble. The water model employed was SPC/E. The OPLS-AA force field was used with van der Waals and short-range electrostatic interactions were truncated at 1.2 nm, with the long-range electrostatic interactions being treated by the particle mesh Ewald method. It is important to mention that in experimental situations it is the electrostatic potential that is controlled, not the charge density. In that sense, it would be intuitive to run simulations at constant potential instead of constant charge. However, the computational cost required as well as the difficulties of implementing this technique justify the use of a more simplified model. In order to make the modeling more simple and yet realistic, we adopted the use of different surface charge densities on the electrodes from $\sigma_s = 0$ (discharged ultracapacitor) to $\sigma_s = \pm 4.8 \mu C cm^{-2}$) to mimic the applied potentials, which was also used by other simulation studies.[6-11] With this procedure we ensure that all comparisons can be made with the supercapacitors to the same given potential. To obtain the electrostatic potential profiles the one-dimensional Poisson equation was solved numerically, as described in detail in our previous works:[12, 13]

$$\Phi(z) = -\frac{1}{\varepsilon_0}\int_{-z_0}^{z} (z - z')\rho_z(z')dz' \qquad \text{(eq. S4)}$$

where $\rho_z(z')$ is the local charge density due to the atomic charge distribution of each ionic species.From the electrostatic potential, we can obtain the capacitance integral (C_I) and differential (C_D). For this, we determine the total potential drop in devices as $\Delta\Delta\Phi = \Delta\Phi^{carg} - \Delta\Phi^{descarg}$where$\Delta\Phi = \Phi^{cathode} - \Phi^{anode}$is calculated for uncharged and charged electrode. In this way thecapacitances (differential and integral) can be obtained (see main text).

Quantum properties for the SVD and pyridinic systems

Density of states (DOS)

SVD

In the SVD–N configuration, it is observed that the bond distance C-C = 1.39-1.45 Å and C-N =1.33-1.37 Å. As shown in Figure 3(c), the state density near the Fermi level increases with functionalization and there is an EF displacement of approximately 0.06 eV below the Dirac cone, due to having fewer electrons compared to the pristine model, denoting the model an electron-accepting nature (*p-type*). The energy gap between valence and conduction bands is equal to 0.48 eV. The forming energy of the model is equal to 0.39 eV/Å, in good agreement with literature.[14] SVD-F has distances of C-C=1.38-1.44 Å and C-F=1.52-1.53 Å. The C-F bond is identified to be considerably greater than C-N. This profile may be related strong bond of the fluorine atom and the sp3 hybridization with the carbon atom.[15] In Figure 3(e) it is possible to identify the change in DOS compared to pristine graphene. Because the model has more electrons than pristine graphene, the Fermi level shifts slightly above the Dirac cone (0.004 eV), assigning an *n-type* character to the model. The gap between valence and conduction bands is 0.6 eV. The formation energy is 0.64 eV/Å, having lower energy stability compared to the same nitrogen doped model. SVD-S has distances between C-C = 1.41-1.46 Å and C-S = 1.66-1.70 Å is ~16% longer than that of the C-C bond of graphene pristine (1.47 Å). According to Figure 3(g), the state density of this configuration differs only from the pyrrolic configuration due to the emergence of electronic states near -0.3 eV energy. The state peak comes from the dangling bond -C of the model. The calculated gap is 0.18 eV and the Fermi level shifts 0.05 eV above the Dirac cone, giving *n-doping* to the configuration. The E_{FOR} of the model is 0.47 eV/Å, being more stable than previous models described. Finally, for SVD-B the calculated bonds distances are C-C = 1.41-1.44 Å and C-B =1.49-1.51 Å. Figure 3(i) shows that increased doping concentration, increase state density contribution close to the EF when compared to the B-Pyrrolic model. The gap entre valence e conduction bands is 0.33 eV and the Fermi level has a displacement of 0.66 eV below the Dirac cone, characterizing an electron acceptor doping nature (*p-type*). The formation energy of the defect is exothermic with a value of -0.5 eV/Å, being the most energetically stable SVD-X model.

Pyridinic

Similar to SVD-N, the N-Pyridinic bonds are C-C = 1.45-1.46Å and C-N = 1.34 Å. In Figure 3(c) the N-Pyridinic DOS presents state density change near the Fermi level energy compared to pristine graphene. There are peaks in the density of electronic states close to the Fermi level resulting from nitrogen doping, the Fermi level displacement of 0.21 eV below Dirac cone, indicating *p-type* doping with gap between 0.48 eV bands.TheE_{FOR} is 0.24 eV/Å, proving to be more energy stable than the N-Pyrrolic and SVD-N configurations. Pyridine-F shows C-C=1.36-1.39 Å and C-F = 1.51-1.55 Å bonds. The DOS shows the emergence of state density peaks near the EF and conduction band (Figure 3(e)). The gap between the valence and conduction bands is ~ 1.0 eV and the Fermi level displacement is 0.08 eV above the Dirac cone, thus attributing to the model *n-type* doping. The formation energy of the functionalization is 0.58 eV/Å, note that the increased concentration of doping and consequently the absence of dangling bond C, contributes to the energetic stability of the sheet compared to Pyrrolic and SVD models.Pyridinic-S shows C-C = 1.42 Å and C-S = 1.66Å bonds. In Figure 3(g) shows the model DOS where the emergence of electronic state peaks near Fermi level is identified, significantly increasing the state density compared to S-Pyrrolic and SVD-S. A gap between the bands of 0.25 eV is evidenced and a Fermi level shift of 0.7 eV above the Dirac cone, retaining *type n* doping. The defect formation energy is equal to 0.44 eV /Å, being more energetically favorable when compared to the SVD-S configuration. However, sulfur-doped pyrrolic configurations have lower defect formation energy (0.34

eV/Å). However, no electronic states are identified near the EF (Figure 3(g)). Thus, the Pyridinic-S configuration stands out as the most favorable one, since it presents an increase in DOS close to EF and low formation energy. Ultimately, boron doping results in bonds of C-C =1.42 and C-B=1.51-1.52 Å, in agreement with previous studies.[15] The model DOS is presented in Figure 3(i), due to the functionalization it is possible to identify the increase of state density close to the EF. The Pyridinic-B gap present energy of 0.25 eV, whereas the Fermi level moves below the Dirac cone with energy of approximately 1.0 eV, thus attributing a *p-type* doping to the graphene. The defect formation energy of this configuration is equal to -1.22 eV/Å, being more stable compared to all models investigated in this study.

As noted, the structural and chemical modifications of graphene directly interfere with its electronic properties. This change is desirable because it can add the quantum capacitance of the material from its electronic state density as described below.

Capacitance quantum

Fluorine doping

Fluorine-doped Pyrrolic, SVD and Pyridinic models at $\varphi = 0$ V equals 34, 15 and 44 μF/cm², respectively (Figure 3(f)). Pyridinic C_Q increased approximately 50-fold over pristine graphene to the same potential. Pyrrolic maximum C_Q, SVD and Pyridinic are equal to 41 μF/cm² (0.07 V), 158 μF/cm² (0.21 V) and 209 μF/cm² (-0.12 V), respectively. In Figure 3(f) shows the C_Q performance along the potential window for the Pyrrolic model. On the other hand, SVD has high C_Q in positive potentials, enabling its performance as a positive electrode in asymmetric capacitors. However, in the case of Pyridinic above, its high C_Q is pronounced in negative potentials. For potentials above 0.1 V, your C_Q is zero. The low C_Q in this range comes from the Dirac cone gap below

0.1 eV as shown in Figure 3(e). Because it is more energy stable and has a high C_Q> 200 μF/cm², the Pyridinic model is promising to act as a negative electrode in asymmetric electrochemical capacitors, since its high capacitance is verified in negative potentials. Unlike doping with N, doping with F presents different possibilities of electrode actuation. This behavior is related to the existence of electronic peaks in the valence or conduction band of the models (Figure 3(e)), which directly affect the position of the C_Q peaks, as shown in Figure 3(f).

Sulfur doping

In Figure 3(h) shows the C_Q curves of sulfur-doped models. Note that the V-curve profile of the Pyrrolic model is similar to pristine graphene. This behavior is related to its DOS profile, which shows no electronic changes close to Fermi energy, resembling the pristine graphene DOS (Figure 3(g)). The C_Q value of the Pyrrolic, SVD and Pyridinic models at $\varphi = 0$ V is equal to 0.9, 4.5 and 75 μF/cm², respectively. Similar to pristine graphene, Pyrrolic's maximum C_Q is approximately 21 μF/cm² at -0.6 V, however with increasing doping, the maximum C_Q has a five-fold increase in value for the SVD and Pyridinic models, with values equal to 130 μF/cm² (0.33 V) and 105 μF/cm² (-0.15 V), respectively. SVD is found to have maximum C_Q in positive potentials, while Pyridinic has maximum C_Q in negative potentials. Therefore, it may be suggested that SVD is promising to act as a positive electrode in asymmetric electrochemical capacitors, while Pyridinic is promising as a negative electrode.

Boron doping

The boron-doped Pyrrolic, SVD and Pyridinic models, when subjected to $\varphi = 0$ V, have C_Q equal to 56, 0.9 and 94 μF/cm², respectively (Figure 3(j)). It is observed that SVD at 0 V, presents C_Q value close to that of pristine graphene. This is due to the presence of the gap near Fermi energy (Figure 3(i)) there are no electronic states in this region. Pyrrolic, SVD and Pyridinic models have a maximum C_Q of 170 μF/cm² (-0.15 V), 90 μF/cm² (0.33 V) and 94 μF/cm² (0 V). Note that C_Q dramatically decreases to zero for potentials above 0.2 V for the Pyrrolic model and - 0.2 V for the Pyridinic model. This behavior is derived from the gap observed in the DOS profile of the models at energies below -0.2 eV (Pyrrolic) and above 0.2 eV (Pyridinic), as shown in Figure 3(i). SVD and Pyridinic show maximum C_Q on the positive side of the potential window, suggesting promising positive electrodes in asymmetric electrochemical capacitors. Pyrrolic offers maximum C_Q for window negative potentials and may be suggested as promising in acting as a negative electrode.[16]

EDL – ADDITIONAL ANALYSIS.

Density Profiles

In general, cations have a typical numerical density fluctuation in EDL for all cases (Figure S2). This oscillatory pattern, which extends beyond the electrode surface, is not observed for anions that have a higher relative structure, characterized by the difference in height at the first peak of each profile. In uncharged electrodes (Figure S3), our results suggest that the accumulation of ions does not depend on doping of graphene. In addition, the SO_4^{2-} anion as well as water molecules show a strong presence on the surface of positively charged and discharged electrodes, indicated by comparable heights of the first peaks located at ~1.2 nm. In negatively charged electrodes, as expected, we observed a shift of peaks to SO_4^{2-} ions as cations accumulate above the first hydration layer on the considered surfaces. This effect is most pronounced for the fluorine-doped graphene electrode. In addition, as the electrode is positively charged (Figure S4), cation density decreases while anion density increases.

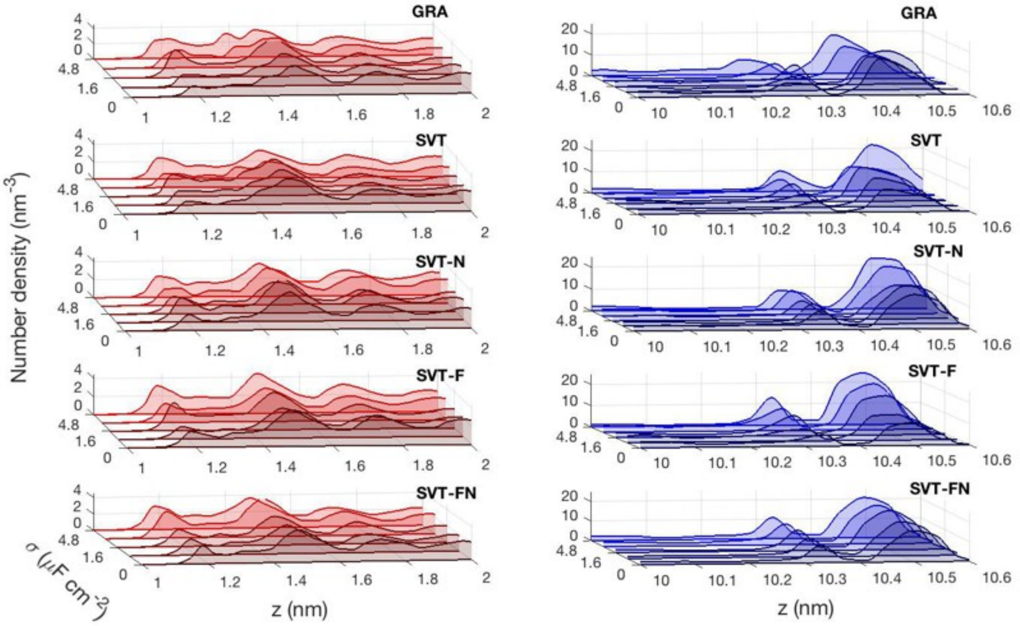

Figure S2. Number ion densities (in nm^{-3}) of cations (in red) and anions (in blue) near the negative and positive electrodes, respectively. The distributions are presented as a function of the charge density magnitude (μCcm^{-2}) and of distance between electrodes, z (nm).

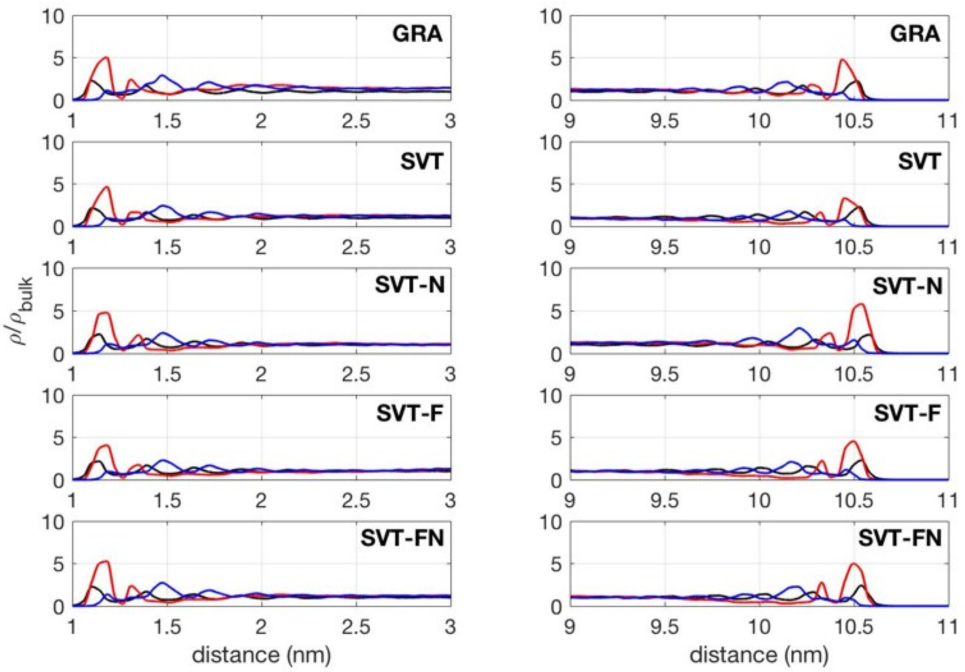

Figure S3. Number densities (in nm^{-3}) of cations (in blue), anions (in red) and water (in black) at σ = 0.

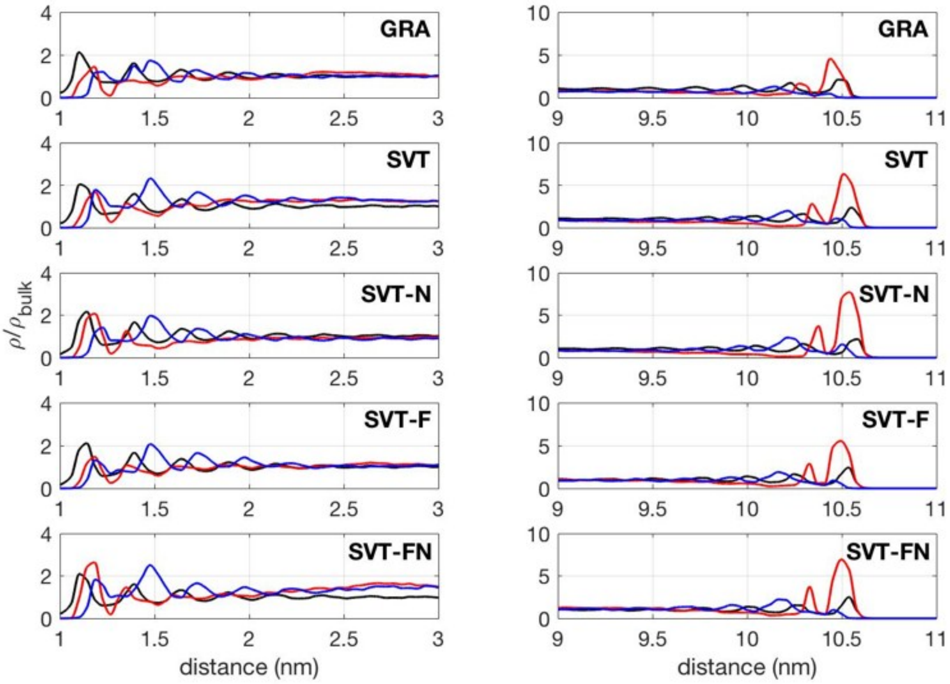

Figure S4. Number densities (in nm^{-3}) of cations (in blue), anions (in red) and water (in black) at $\sigma = 4.8$.

Electrode-Electrolyte Energy

Figure S5 allows quantifying the characteristic electrodes asymmetry in terms of the total energy interaction between the electrolyte and the positive (green bars) and negative (red bars) electrodes. This energy is higher for nitrogen-doped graphene and is consistent with simulation snapshots, which shows a noticeable increase in anionic density in the interfacial layer of the positively charged electrode. Unlike that observed for ionic liquids, the aqueous electrolyte ion interacts more strongly with the positive electrode, since the anion has a larger number of both electrostatic and van der Waals interaction sites as discussed in the main text.

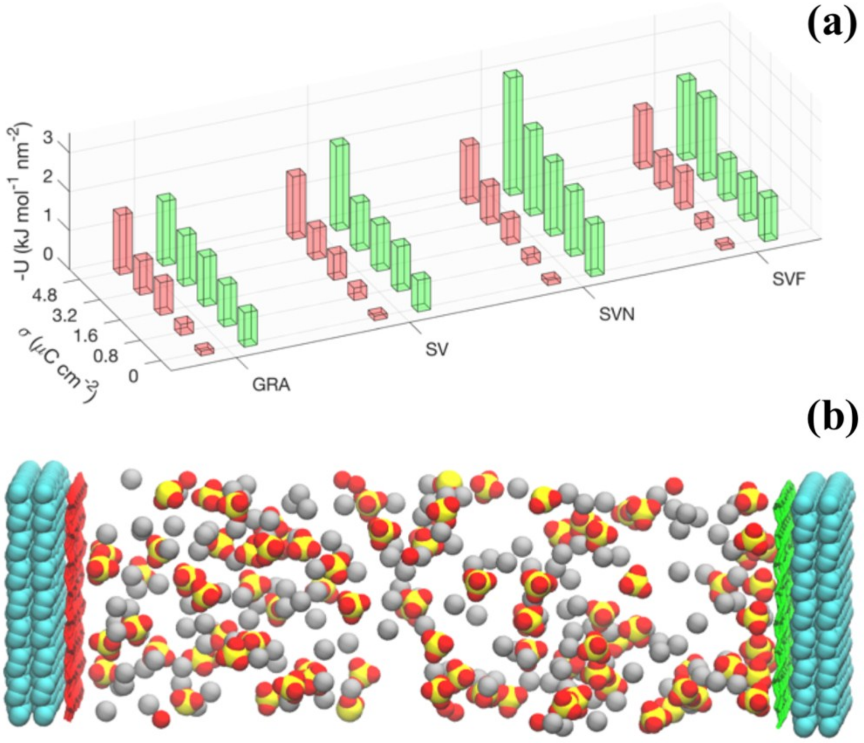

Figure S5: At the top, interaction energy anion-positive electrode (green bars) cation-negative electrode (red bars). All energies are normalized by the electrode surface area. Values in panel a) were multiplied by -1 for the sake of clarity. Below, representative simulation snapshots for $LiSO_4$ ions accumulating near asymmetric supercapacitor negative electrode (left) and positive (right). These electrodes are charged at σ = 4.8μC/cm^2. Water is omitted for clarity.

Table S1: EDL differential capacitance (in μF/cm^2), electrochemical potential (in V) and charge density (in μC/cm^2), determined point by point for each of the investigated supercapacitors.

	GRA		SV		SVN		SVF		AFN	
Φ (V)	σ	C_D	σ	C_D	σ	C_D	σ	C_D	σ	C_D
-0.5	-3.8	7.6	-3.7	7.4	-3.6	7.2	-3.6	7.2	-3.9	7.8
-0.4	-3.1	7.7	-3.0	7.5	-2.9	7.3	-3.0	7.4	-3.2	8.0
-0.3	-2.4	8.0	-2.3	7.7	-2.3	7.6	-2.3	7.7	-2.5	8.4
-0.2	-1.7	8.5	-1.6	8.1	-1.6	8.1	-1.6	8.2	-1.9	9.3
-0.1	-1.0	10.0	-0.9	9.2	-1.0	9.7	-1.0	9.9	-1.2	11.7
0.1	0.4	3.9	0.5	4.7	0.3	3.3	0.3	3.3	0.2	1.9
0.2	1.1	5.4	1.2	5.8	1.0	4.9	1.0	4.9	0.9	4.3
0.3	1.8	5.9	1.9	6.2	1.6	5.5	1.6	5.5	1.5	5.1
0.4	2.5	6.2	2.6	6.4	2.3	5.7	2.3	5.8	2.2	5.6
0.5	3.2	6.3	3.2	6.5	2.9	5.9	3.0	5.9	2.9	5.8
0.6	3.9	6.4	3.9	6.6	3.6	6.0	3.6	6.0	3.6	6.0
0.7	4.6	6.5	4.6	6.6	4.2	6.1	4.3	6.1	4.3	6.1
0.8	5.3	6.6	5.3	6.7	4.9	6.1	4.9	6.2	4.9	6.2

0.9	5.9	6.6	6.0	6.7	5.6	6.2	5.6	6.2	5.6	6.2
1	6.6	6.6	6.7	6.7	6.2	6.2	6.2	6.2	6.3	6.3

Table S2: EDL integral capacitance (in μF/cm^2), electrochemical potential (in V) and charge density (in μC/cm^2). Note that the values of the charge densities assigned to the electrodes covers a range of 1.5 V.

	GRA		SV		SVN		SVF		AFN	
ΔΔΦ (V)	σ	C_I	σ	C_I	σ	C_I	σ	C_I	σ	C_I
0.1	0.5	5.2	0.5	5.2	0.3	3.4	0.4	3.6	0.4	4.0
0.2	0.9	4.3	0.9	4.3	0.7	3.3	0.7	3.5	0.7	3.7
0.3	1.2	4.0	1.2	4.0	1.0	3.3	1.0	3.4	1.1	3.6
0.4	1.5	3.9	1.5	3.8	1.3	3.3	1.3	3.4	1.4	3.6
0.5	1.9	3.8	1.9	3.7	1.7	3.3	1.7	3.4	1.8	3.6
0.6	2.2	3.7	2.2	3.6	2.0	3.3	2.0	3.3	2.1	3.5
0.7	2.6	3.7	2.5	3.6	2.3	3.3	2.3	3.3	2.5	3.5
0.8	2.9	3.6	2.9	3.6	2.6	3.3	2.7	3.3	2.8	3.5
0.9	3.3	3.6	3.2	3.5	3.0	3.3	3.0	3.3	3.2	3.5
1	3.6	3.6	3.5	3.5	3.3	3.3	3.3	3.3	3.5	3.5
1.1	3.9	3.6	3.9	3.5	3.6	3.3	3.7	3.3	3.9	3.5
1.2	4.3	3.6	4.2	3.5	4.0	3.3	4.0	3.3	4.2	3.5
1.3	4.6	3.6	4.5	3.5	4.3	3.3	4.3	3.3	4.5	3.5
1.4	5.0	3.6	4.8	3.5	4.6	3.3	4.6	3.3	4.9	3.5
1.5	5.3	3.5	5.2	3.5	5.0	3.3	5.0	3.3	5.2	3.5

References

1. C. Zhan, J. Neal, J. Wu and D.-e. Jiang, *The Journal of Physical Chemistry C*, 2015, **119**, 22297-22303.
2. E. Paek, A. J. Pak, K. E. Kweon and G. S. Hwang, *The Journal of Physical Chemistry C*, 2013, **117**, 5610-5616.
3. J. Vatamanu, X. Ni, F. Liu and D. Bedrov, *Nanotechnology*, 2015, **26**, 464001.
4. C. Zhan, Y. Zhang, P. T. Cummings and D. E. Jiang, *Phys Chem Chem Phys*, 2016, **18**, 4668-4674.
5. P. Hirunsit, M. Liangruksa and P. Khanchaitit, *Carbon*, 2016, **108**, 7-20.
6. M. Wu, W. Li, S. Li and G. Feng, *RSC Advances*, 2017, **7**, 28945-28950.
7. Y. Shim, Y. Jung and H. J. Kim, *The Journal of Physical Chemistry C*, 2011, **115**, 23574-23583.
8. R. Kalluri, T. Ho, J. Biener, M. Biener and A. Striolo, *The Journal of Physical Chemistry C*, 2013, **117**, 13609-13619.
9. T. A. Ho and A. Striolo, *J Chem Phys*, 2013, **139**, 204708.
10. S. Zhang, Z. Bo, H. Yang, J. Yang, L. Duan, J. Yan and K. Cen, *Journal of Power Sources*, 2016, **334**, 162-169.
11. G. Feng, S. Li, W. Zhao and P. T. Cummings, *AIChE Journal*, 2015, **61**, 3022-3028.

12. A. Neto and E. Fileti, *Journal of Molecular Liquids*, 2019, **292**, 111439.
13. A. J. P. Neto and E. E. Fileti, *The Journal of Physical Chemistry C*, 2018, **122**, 21824-21832.
14. Y. Taluja, B. SanthiBhushan, S. Yadav and A. Srivastava, *Superlattices and Microstructures*, 2016, **98**, 306-315.
15. X. Wang, G. Sun, P. Routh, D.-H. Kim, W. Huang and P. Chen, *Chemical Society Reviews*, 2014, **43**, 7067-7098.
16. S. M. Mousavi-Khoshdel and E. Targholi, *Carbon*, 2015, **89**, 148-160.